

Chondroinductive Alginate-Based Hydrogels Having Graphene Oxide for 3D Printed Scaffold Fabrication

Felipe Olate-Moya,* Lukas Arens, Manfred Wilhelm, Miguel Angel Mateos-Timoneda, Elisabeth Engel, and Humberto Palza*



Cite This: *ACS Appl. Mater. Interfaces* 2020, 12, 4343–4357



Read Online

ACCESS |



Metrics & More



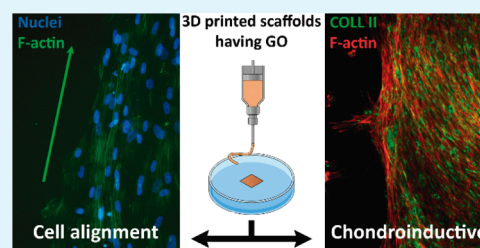
Article Recommendations



Supporting Information

ABSTRACT: Scaffolds based on bioconjugated hydrogels are attractive for tissue engineering because they can partly mimic human tissue characteristics. For example, they can further increase their bioactivity with cells. However, most of the hydrogels present problems related to their processability, consequently limiting their use in 3D printing to produce tailor-made scaffolds. The goal of this work is to develop bioconjugated hydrogel nanocomposite inks for 3D printed scaffold fabrication through a micro-extrusion process having improved both biocompatibility and processability. The hydrogel is based on a photocrosslinkable alginate bioconjugated with both gelatin and chondroitin sulfate in order to mimic the cartilage extracellular matrix, while the nanofiller is based on graphene oxide to enhance the printability and cell proliferation. Our results show that the incorporation of graphene oxide into the hydrogel inks considerably improved the shape fidelity and resolution of 3D printed scaffolds because of a faster viscosity recovery post extrusion of the ink. Moreover, the nanocomposite inks produce anisotropic threads after the 3D printing process because of the templating of the graphene oxide liquid crystal. The *in vitro* proliferation assay of human adipose tissue-derived mesenchymal stem cells (hADMSCs) shows that bioconjugated scaffolds present higher cell proliferation than pure alginate, with the nanocomposites presenting the highest values at long times. Live/Dead assay otherwise displays full viability of hADMSCs adhered on the different scaffolds at day 7. Notably, the scaffolds produced with nanocomposite hydrogel inks were able to guide the cell proliferation following the direction of the 3D printed threads. In addition, the bioconjugated alginate hydrogel matrix induced chondrogenic differentiation without exogenous pro-chondrogenesis factors as concluded from immunostaining after 28 days of culture. This high cytocompatibility and chondroinductive effect toward hADMSCs, together with the improved printability and anisotropic structures, makes these nanocomposite hydrogel inks a promising candidate for cartilage tissue engineering based on 3D printing.

KEYWORDS: 3D printing, graphene oxide, liquid crystals, hydrogels, chondrogenesis



INTRODUCTION

Additive manufacturing such as 3D printing is an emerging tool for biomedical applications in regenerative therapies.¹ Particularly, 3D printed scaffolding is a versatile method to obtain tailor-made structures for tissue engineering and 3D cell culture.² Among different biomaterials used for scaffold fabrication, hydrogels based on natural polymers have outstanding characteristics such as high water content, porosity, softness, biocompatibility, and bioactivity.^{2,3} In addition, the properties and characteristics of these biopolymers can be modified through physical/covalent crosslinking or bioconjugation.⁴ From the 3D printing perspective, scaffolds based on alginate (ALG) have been widely studied because of its ability to change quickly from a viscous fluid state (an ALG solution) to a more-rigid hydrogel, by an isotropic cross-linking process between α -D-glucuronic acid residues from the polymer chains and divalent cations.⁵ From the biological perspective, the inherent lack of proper biocompatibility and bioactivity of ALG has led to the strategy to combine this biopolymer with bioactive hydrogels such as gelatin (GEL) or

its derivatives for biomedical applications.⁶ The purpose of this bioconjugation is to mimic the composition, microstructure, and mechanical properties of the extracellular matrix (ECM) of a determined tissue.⁷ GEL, particularly the photocrosslinkable derivative methacryloyl GEL (GEL-MA), is often used for this purpose and for 3D printing.⁸ GEL is a polypeptide of animal origin, obtained from the hydrolysis of collagen that is found in the ECM of most animal tissues. Scaffolds based on GEL have shown high cell viability, proliferation, and cell attachment because of the arginylglycylaspartic acid (RGD) amino acid sequence existing in its polymeric chains.⁹ For instance, scaffolds fabricated from blends of ALG/GEL displayed enhanced cell proliferation compared with pure ALG

Received: December 5, 2019

Accepted: January 7, 2020

Published: January 7, 2020



scaffolds.¹⁰ Therefore, GEL and its derivatives appear as an easy and economic method of bioconjugation.^{9,11}

Among the different potential applications of 3D printed hydrogel scaffolds, several studies have focused on cartilage tissue engineering during the last decade.¹² Cartilage is a tissue formed by cells called chondrocytes. It is characterized by a lack of vascularization of its ECM and a poor regenerative capacity; so the injuries on this kind of tissue are difficult to treat.¹³ The ECM of cartilage (based on articular cartilage) consists of about 65–80% of water, which is in the same range as hydrogels. Considering the dry weight, the principal components of the cartilage are collagen (up about 60%) and proteoglycans (PGs; 30–40%) consisting of proteins covalently bonded to glycosaminoglycans (GAGs).¹⁴ These GAGs are highly negatively charged polysaccharides consisting of a disaccharide repeating unit with an amino sugar moiety bonded to an uronic sugar of a galactose moiety.¹⁵ With the aim of mimicking the ECM of cartilage tissues, previous evidence reports the use of GAGs as part of a hydrogel network in scaffolds.¹⁶ Among the different GAGs usually employed for these hydrogel scaffolds, hyaluronic acid, heparin, heparan sulfate, and chondroitin sulfate (CS) stand out.¹⁷ From these three biopolymers, CS has a great potential for cartilage tissue engineering because of its chondrogenic properties and low costs.¹⁸ CS is found in the ECM of cartilage covalently linked to a protein, forming aggrecan, the main PG of this type of tissue. Aggrecan has the ability to interact with hyaluronic acid chains forming PG aggregates, which act like a hydrogel structure, able to retain water molecules maintaining the hydration of the cartilage ECM.¹⁵ Scaffolds based on CS can be formed either by mixing it with other polymer or by crosslinking it covalently with other polymeric chains to form the hydrogel network.^{19–21} From the regenerative therapy point of view, the engineered chondral tissue employing human mesenchymal stem cells (hMSCs) for chondrocyte phenotype differentiation is an attractive option for the treatment of cartilage injuries.²² Therefore, GEL/CS-bioconjugated hydrogel scaffolds having hMSCs seem to be a proper approach for the design of biomaterials for cartilage tissue engineering.^{23,24} However, despite the good behaviors of ALG, GEL, and CS for cartilage regeneration, scaffolds based on covalently bonded ALG–GEL–CS ternary hydrogels and manufactured by 3D printing has not yet been studied.

3D printing of scaffolds based on hydrogels has a series of complications related to its poor mechanical properties and low processability.²⁵ These difficulties have motivated the development of reinforced hydrogels with nanomaterials like metallic nanoparticles, hydroxyapatite, clay, and carbon-based nanomaterials.²⁶ These nanocomposites do not only improve the hydrogel mechanical behavior but also their rheological properties, usually showing additional attributes such as optical properties, anisotropic characteristics, and bioactivity.²⁷ One of the most interesting nanoparticle for bioapplications is graphene oxide (GO), a graphite derivative based on one or only a few layers of aromatic sp²-hybridized carbon atoms, which are partially functionalized with oxygen-rich groups (mainly carboxylic acid, hydroxyl, and epoxy groups).²⁸ As a result of the polarity of its oxidized functional groups, GO is very stable in water suspensions unlike the hydrophobic graphene, reduced GO, and carbon nanotubes. This property makes GO suitable for biomedical applications such as drug delivery, biosensors, phototherapy, and tissue engineering.²⁹ For instance, nowadays, it is well-known that hydrogel/GO

nanocomposite hydrogels exhibit enhanced mechanical properties compared to pure hydrogels.³⁰ When the polymers used for the hydrogels have hydrogen donor/acceptor functional groups in their structure (e.g., amido, hydroxy, amino, or carboxyl groups), GO can further act as a physical crosslinker by multiple hydrogen bond interactions.³¹ This characteristic could explain the superior mechanical properties of GO nanocomposite hydrogels. Another relevant feature of GO is its bioactivity,²⁹ motivating its incorporation into biomaterials for antimicrobial purposes. Several antimicrobial polymer/GO nanocomposites have been produced based on different bactericidal mechanisms proposed for pure GO.³² Regarding the mesenchymal stem cell (MSC) response, scaffolds based on polymer/GO nanocomposites have been mainly prepared to analyze their osteogenic effect,³³ although the MSCs differentiation to other cell phenotypes has also been explored over the last years.²⁹ Indeed, biomaterials based on GO can further enhance neurogenic,³⁴ adipogenic,³⁵ and chondrogenic³⁶ differentiation. The recent work by Zhou et al. is of particular interest, where a photocrosslinkable hydrogel bioink based on GEL-MA, poly (ethylene glycol) diacrylate, and GO was used for 3D bioprinting scaffolds. The presence of GO in the printed MSC-loaded constructs increased the cell viability and the chondrogenic marker expression.³⁷ These results show a promising future of GO-containing hydrogels in cartilage regenerative medicine applications. The usual approach for the chondrogenic differentiation of MSCs in cartilage tissue engineering is the employment of a biochemical cocktail as a chondrogenic medium. These pro-chondrogenesis agents include transforming growth factor- β (TGF β), dexamethasone, ascorbic acid, and sodium pyruvate, among other supplements.³⁸ In particular, TGF β is a family of cytokines which play a mediator role of signaling cascades for chondrogenic differentiation and retaining the differentiated chondrocyte phenotype.³⁹ However, the use of TGF β as a chondrogenic supplement for hMSCs could take undesired pathways such as osteogenic and hypertrophic chondrocyte differentiation,⁴⁰ tumorigenesis, and metastasis in human cancer.⁴¹ These aspects are part of the issues related with MSC therapy. Therefore, the development of regenerative therapy methods free of exogenous growth factors is necessary for safer and less expensive clinical translation of tissue engineering.

Herein, a novel nanocomposite hydrogel based on a crosslinked network of ALG, CS, and GEL filled with GO is developed as ink for 3D printing scaffold fabrication. The effect of ink composition on printing quality, cytocompatibility, and the intrinsically chondroinductive effect of scaffolds was evaluated varying the GO concentration in the inks.

■ EXPERIMENTAL SECTION

Materials and Reagents for Hydrogel Nanocomposite Synthesis. The biopolymers alginic acid sodium salt from brown algae (ALG), CS type A sodium salt from bovine trachea, and GEL type A from porcine skin BioReagent grades were purchased from Sigma-Aldrich (Norway, China and USA respectively) and used as received. 2-Aminoethyl methacrylate hydrochloride (AEMA), *N*-(3-dimethylaminopropyl)-*N'*-ethylcarbodiimide hydrochloride (EDC), *N*-hydroxysuccinimide (NHS), 2-(*N*-morpholino)ethanesulfonic acid (MES), methacrylic anhydride (MAA), 2-hydroxy-4'-(2-hydroxyethoxy)-2-methylpropiophenone photoinitiator (PI), graphite, potassium permanganate, sodium nitrate, calcium chloride, sulfuric acid, hydrogen peroxide, ethanol, and deuterium oxide were purchased from Sigma-Aldrich or Merck, Millipore. Dialysis tube Spectra/Por 1 (MWCO = 6–8 kDa, 50 mm flat width) utilized in the purification of

methacrylated biopolymers was purchased from Spectrum Laboratories. Type I (ultrapure) water was used for synthesis and purification.

Spectroscopic Characterization. Attenuated total reflection Fourier transform infrared spectroscopy (ATR–FTIR) spectra were acquired from an Agilent Cary 630 FTIR spectrometer. The Raman spectroscopy study was carried out on a HORIBA HR Evolution micro-spectrometer coupled to an Olympus optical microscope with a 100× objective, using a 532 nm laser, 107 mW source power, and using the LabSpec6 software to acquire the spectrograms (three scans accumulated with 90 s of acquisition). Proton NMR analysis was performed on a Bruker AVANCE III HD-400 spectrometer, experiments were measured to solutions of samples in deuterium oxide, and the obtained FID data were processed with MestReNova. The UV–vis spectrum of GO was obtained using a Rayleigh UV-1601 spectrophotometer (10 mm optical path quartz cuvette).

Microstructural Characterization. X-ray diffraction (XRD) measurements were taken using Cu K α radiation with a Bruker D8 Advance diffractometer. Transmission electron microscopy (TEM) images were acquired with a FEI Tecnai F20 S/TEM electron microscope, mounting the sample on a Holey Carbon on 300 mesh Cu grid. Field emission scanning electron microscopy (FE-SEM) images were acquired with a FEI Quanta™ FEG SEM electron microscope. To measure the GO sheet lateral size, a silicon wafer (50 mm of diameter) was treated with plasma and spin coated with 200 μL of 50 $\mu\text{g mL}^{-1}$ of aqueous suspension of GO at 1500 rpm during 2 min. The lateral size distribution was measured by FE-SEM image analysis of this silicon wafer coated with GO, using ImageJ software.

Optical Microscopy Characterization. Polarized light microscopy (POM) studies were performed on a Leica DMLS microscope equipped with a polarizer/analyzer system and a full-wave retardation plate. Cell culture imaging was performed with a Leica DM IL LED phase contrast/fluorescence microscope. Both instruments were equipped with a Leica MC170 HD digital camera for micro-photography acquisition. Frequency distribution histogram of cells direction was plotted using the directionality plugin in Fiji/ImageJ (ImageJ software, USA).⁴²

Chemical Modification of Biopolymers and Synthesis of GO. The three biopolymers ALG, CS, and GEL were functionalized with polymerizable methacrylate groups to obtain ALG-MA, CS-MA, and GEL-MA, respectively. The photocrosslinking of the methacrylated biopolymers, to bioconjugate ALG with bioactive CS and GEL, was carried out with 2-hydroxy-4'-(2-hydroxyethoxy)-2-methylpropiophenone radical PI at 0.05% (w/v). GO was synthesized by a modified Hummers' method from graphite powder.

General Procedure for the Synthesis of ALG-MA and CS-MA. ALG and CS polysaccharide chains were chemically modified with 2-amidoethyl methacrylate moieties, by means of EDC/NHS amidation chemistry.⁴³ For this, 1 g of polysaccharide (ALG or CS) was dissolved in 100 mL of MES 50 mM (pH = 6.5) buffer solution containing NaCl 0.5 M. Then, 0.87 g (4.6 mmol) of EDC and 0.26 g (2.3 mmol) of NHS were added to activate the carboxylic acid groups. After five minutes of activation, 0.38 g (2.3 mmol) of AEMA was added to the mixture, and it is allowed to react for 24 h at room temperature. Next, the methacrylated polymer was precipitated in absolute ethanol; the solid product was separated by vacuum filtration and dried in a vacuum oven at 70 °C overnight. The dry product was dissolved in deionized water, and the solution obtained was dialyzed in a Spectra/Por 1 tube against deionized water for 4 days (changing the dialysate water every 12 h). Finally, the purified product was lyophilized with a Martin Christ Alpha 1-2 LDplus freeze-dryer and stored at –20 °C until its utilization. The ALG-MA and CS-MA synthesized were characterized by FTIR spectroscopy and ¹H NMR spectroscopy.

General Procedure for the Synthesis of GEL-MA. GEL was chemically modified with methacryloyl (MA) functionalities by the widely employed biphasic reaction with MAA.⁴³ Briefly, 1 g of GEL was dissolved in 10 mL of phosphate buffered saline (PBS) at pH = 7.4 and 50 °C. When the solid was completely dissolved, 0.65 mL (4.4 mmol) of MAA was added dropwise under vigorous stirring (300 rpm). The reaction was maintained at 50 °C for 2 h, retaining the pH

value between 7 and 7.5 by the addition of diluted NaOH solution. The mixture was diluted in 90 mL of deionized water and dialyzed in a Spectra/Por 1 tube against deionized water for 4 days (changing the dialysate water after 2 h and then every 12 h). Finally, the purified product was freeze-dried and stored at –20 °C until its utilization. The synthesized GEL-MA was characterized by FTIR spectroscopy and ¹H NMR spectroscopy.

Synthesis of GO. GO was synthesized according to the modified Hummers' method.⁴⁴ First, graphite powder (1.0 g) and sodium nitrate (0.5 g) were mixed, followed by the addition of 25 mL of concentrated sulphuric acid under constant stirring. After 30 min, KMnO₄ (3.0 g) was added gradually to the above solution while keeping the temperature below 20 °C using an ice bath. The mixture was stirred at 35 °C for 2 h, and the resulting solution was diluted by adding 500 mL of water under vigorous stirring during 1 h. To ensure the completion of the reaction with KMnO₄, the suspension was further treated with 30% H₂O₂ solution (5 mL). The resulting mixture was centrifuged and washed with HCl and H₂O, respectively, followed by filtration. The solid residue was resuspended in deionized water, mechanically exfoliated for 1 h with a Vibra-Cell Ultrasonic Processors VC 505 (Sonics & Materials) and freeze-dried to obtain GO sheets. The synthesized GO was characterized through FTIR spectroscopy, UV–visible spectroscopy, POM, TEM, and XRD.

3D Printing of Scaffolds. To fabricate the scaffolds by 3D printing, three inks were formulated: ACG composed by ALG 10 mg mL⁻¹ + ALG-MA 6 mg mL⁻¹ + CS-MA 6 mg mL⁻¹ + GEL-MA 6 mg mL⁻¹ + PI 0.5 mg mL⁻¹, ACG/GO0.1 with the ACG composition + GO 0.1 mg mL⁻¹ and ACG/GO1 with the ACG composition + GO 1 mg mL⁻¹. The 3D printing of scaffolds was carried out in a fourth generation 3D Bioplotter (EnvisionTEC, Germany). Scaffolds were designed using the Materialise Magics software, and the STL files were processed with the Perfactory software. To print the scaffolds, polyethylene cartridges of 30 cm³ (Optimum Components, Nordson EFD) were filled with the inks. The cartridge having the ink was placed in a low-temperature dispensing head at 5 °C, and the ink was extruded through a 25 G needle into a Petri dish at 2 °C. The ink was physically crosslinked by an ionotropic process with a CaCl₂ 100 mM solution (ALG chains) and by a thermotropic process (GEL chains). The 3D printed scaffolds were irradiated with a Blak-Ray UV lamp (Ted Pella, USA) with a wavelength of 365 nm and intensity of 9 mW cm⁻² for 5 min (at 20 cm of distance) to photocrosslink the methacrylated biopolymers. Finally, the scaffolds were freeze-dried and stored at –20 °C until its biological evaluation.

Water Content and Swelling Ratio of Scaffolds. In order to measure the water content in the scaffolds and swelling process, ACG, ACG/GO01, and ACG/GO1 scaffolds ($n = 5$) were weighed immediately after ionotropic/photocrosslinking. Then, the scaffolds were freeze-dried, and the mass of each dried hydrogel (xerogel) was determined. Finally, the lyophilized scaffolds were incubated at 37 °C in PBS for 24 h, and the mass of each rehydrated scaffold was measured. The water mass fraction and swelling ratio of the scaffolds were determined by the following equations

$$\text{Water mass fraction} = \frac{m_{\text{H}} - m_{\text{D}}}{m_{\text{H}}}$$

$$\text{Swelling ratio} = \frac{m_{\text{S}} - m_{\text{D}}}{m_{\text{D}}}$$

where m_{H} , m_{D} , and m_{S} represent the mass of hydrated scaffolds, the mass of dried scaffolds, and the mass of scaffolds after swelling in PBS, respectively.

Rheological Characterization. Rheological measurements were carried out on a Discovery Hybrid Rheometer III (TA Instruments) equipped with a Peltier temperature control system. All measurements were performed at 4 °C, and the samples were allowed to reach a state of equilibrium for 60 s prior to each measurement. For the three formulated inks, a cone-plate geometry (40 mm, 2°) was used, and the shear viscosity was measured at shear rates from 0.01 to 1000 s⁻¹. Oscillation amplitude sweeps from 0.1 to 1000 Pa at a frequency of 1 Hz were performed to define the linear viscoelastic region (LVR).

From the LVR, a stress of 10 Pa was chosen for the oscillation frequency measurements conducted at a frequency range of 10^{-3} to 10^2 Hz. For the viscosity recovery tests, the viscosity of the inks was measured for 130 s, while the shear rate was adapted to 0.1 s^{-1} for 60 s in stage I to 100 s^{-1} for 10 s in stage II and again to 0.1 s^{-1} for 60 s in stage III. This procedure was chosen to mimic the printing process and to assess the recovery of the viscosity of the hydrogels. The 100 s^{-1} shear rate was estimated to be the maximum shear rate experienced by the ALG-based hydrogels during the 3D printing process.⁴⁵ The change in moduli during isotropic crosslinking of the inks was measured with a plate–plate geometry (8 mm, gap = 1.4 mm). The measurements were conducted at 0.1% strain and at a frequency of 1 Hz for 800 s. One minute after the measuring started, 0.5 mL of 100 mM CaCl_2 solution was dispensed around the ink causing the crosslinking while the storage and loss moduli were recorded.

Mechanical Properties. The study of mechanical properties of hydrogels was carried out by a uniaxial unconfined compression test using an Electromechanical Universal Testing Machine WDW-55 (Jinan Testing Equipment IE Corporation, China), equipped with a 5 kN load cell. Cylindrical geometries with a diameter of 10 mm and a height of 5 mm were made by pouring the inks in an epoxy resin mold, and the isotropic and subsequent photochemical crosslinking were carried out. The cylinders were cooled at $4 \text{ }^\circ\text{C}$, and mechanical tests were carried out at a compression rate of 1 mm min^{-1} at room temperature. A minimum of 5 samples for each type was tested. The test was performed once a force of 0.05 N was applied to verify the contact with the specimen. The compressive modulus of the scaffolds was determined by calculating the slope of a linear region of the stress–strain curve.

Biocompatibility Evaluation. The biological performance of 3D printed scaffolds was studied using human adipose tissue derived mesenchymal stem cells (hADMSCs) provided by the Texas A&M Health Science Center College of Medicine Institute for Regenerative Medicine at Scott & White (NIH Grant P40RR017447). The hADMSCs were used for alamarBlue and fluorescence staining without further characterization. Following the provider's protocol, cells were expanded at low seeding densities (150 cells/cm^2) in conditioned culture medium (CCM) composed of minimum essential medium alpha (MEM α , Invitrogen) supplemented with 2 mM L-glutamine (Invitrogen), 100 U/mL penicillin (Invitrogen), 100 U/mL streptomycin (Invitrogen), and 16% Hyclone fetal bovine serum (FBS; GE Healthcare). Cells were maintained at $37 \text{ }^\circ\text{C}$ in an atmosphere of 5% CO_2 . During expansion, the medium was refreshed every 3 days.

AlamarBlue Assay. The cell proliferation assay was performed by placing lyophilized scaffolds cut with a biopsy punch (7 mm of diameter) into an ultra-low attachment 24 well plate. The 3D printed scaffolds were sterilized with absolute ethanol for 1 h, thrice washed with PBS, irradiated with UV-C light for 1 h, and preconditioned with 0.5 mL of CCM. Then, hADMSCs (passage 9, 40,000 cells/scaffold) were seeded on the scaffolds and the ALG control and cultured in a final volume of 1 mL of CCM, and the general protocol for alamarBlue assay was carried out at different time points. For this, 100 μL of alamarBlue solution was added to each well and cultured for 2 h at $37 \text{ }^\circ\text{C}$ and 5% CO_2 atmosphere. Once the incubation time was reached, an aliquot of 100 μL was transferred to a 96 well plate, and the fluorescence intensity is measured at 590 nm applying an excitation wavelength of 530 nm in an Infinite 200 PRO multimode microplate reader (Tecan). Each sample was measured in triplicate, and the fluorescence intensities were corrected subtracting the respective blanks without cells.

Fluorescence Staining and Live/Dead Assay. The cell proliferation, viability, morphology, and adhesion to the scaffolds were studied by fluorescence microscopy. Lyophilized 3D printed scaffolds discs of 7 mm were placed on an ultra-low attachment 24 well plate and sterilized as described above.

The analysis of cell adhesion, proliferation, and morphology was performed by nuclei and F actin staining with DAPI (4',6-diamidino-2-phenylindole, Life Technologies) and FITC-phalloidin (Life

Technologies), respectively. After 7 days of hADMSCs (passage 4) culture on 3D printed scaffolds (40,000 cells/scaffold), cells were fixed with 4% paraformaldehyde (Electron Microscopy Sciences) and washed with PBS. Cytoskeletal actin filaments were stained with FITC-phalloidin at 1/200 dilution ($300 \text{ units mL}^{-1}$) in PBS-glycine (PBS-Gly) and incubated for 30 min at room temperature followed by PBS-Gly washing. Next, nuclei staining was carried out by incubation for 10 min at room temperature with DAPI $2 \mu\text{g mL}^{-1}$ in PBS-Gly, followed by PBS-Gly washing. Finally, the samples were analyzed by fluorescence microscopy (each sample in triplicate).

The in vitro cell survival within the scaffolds was studied by Live/Dead assay with calcein-AM (Invitrogen) for live cell staining and propidium iodide (Invitrogen) for dead cell staining. After 7 days of hMSC (passage 6) culture on 3D printed scaffolds (20,000 cells/scaffold), Live/Dead staining of hMSCs on scaffolds was performed after being washed with Dulbecco's PBS saline buffer (DPBS, Invitrogen). For this, scaffolds were incubated in calcein-AM 5 mM/propidium iodide 5 mM in DPBS for 20 min at $37 \text{ }^\circ\text{C}$ and 5% CO_2 atmosphere. Following the incubation time, the samples were washed with DPBS and observed using a fluorescence microscope (each sample in triplicate).

Immunofluorescence Analysis. The immunofluorescence staining of chondrogenic markers for collagen type II, aggrecan, and SOX 9, was performed for hADMSCs (passage 9, 40,000 cells/scaffold) cultured on 3D printed scaffolds after 28 days in CCM. Immunostaining was carried out as follows: scaffolds were washed twice in PBS at $37 \text{ }^\circ\text{C}$, fixed in 4% paraformaldehyde (Electron Microscopy Sciences) for 10 min, and washed twice in PBS. Cells on scaffolds were permeabilized with Triton X-100 (Sigma-Aldrich) 0.25% in PBS-Gly (15 g glycine/100 mL PBS, Sigma-Aldrich) for 10 min, and then they were washed thrice in PBS-Gly. Scaffolds were treated with blocking buffer (6% bovine serum albumin in PBS-Gly, Sigma-Aldrich) for 45 min and incubated overnight at $4 \text{ }^\circ\text{C}$ in rabbit polyclonal antibody against collagen type II (ab34712, 1/100), aggrecan (ab36861, 1/100), or SOX 9 (ab3697, 1:100) (Abcam). After washing them three times in PBS-Gly, the scaffolds were then incubated in a secondary antibody (1/100, Alexa Fluor 488 goat anti-rabbit IgG H&L ab150077, Abcam) for 1 h at room temperature. Nuclei and F actin were counterstained using DAPI stain and TRITC-phalloidin (Life Technologies), respectively, as described above.

Statistical Analysis. The measured data of water content, compression moduli, and alamarBlue assay was expressed as arithmetic mean \pm standard deviation. The analysis of variance (ANOVA) and the Tukey's post-test were performed to assess the statistical significance between groups using OriginPro 8.6 (Origin-Lab) or Prism 6 (GraphPad).

RESULTS AND DISCUSSION

Characterization of the Modified Biopolymers. The different biopolymers (ALG, CS, and GEL) were modified with MA moieties to obtain a high degree of functional groups able to photocrosslink, as reported previously.⁴⁵ The methacrylation of biopolymers was confirmed and quantified by ATR-FTIR and ^1H NMR spectroscopy. Figure 1 shows the FTIR spectra of the three biopolymers before and after methacrylation, where it is possible to observe a shoulder in the spectra of ALG-MA at 1707 cm^{-1} , and a hypsochromic shift of the carbonyl band to 1636 cm^{-1} in CS-MA due to the incorporation of 2-amidoethyl methacrylate groups. In addition, both polysaccharides exhibit their characteristic stretching vibration bands of O–H bonds (around 3300 cm^{-1}), $\text{C}_{\text{sp}^3}\text{–H}$ bonds (around 2900 cm^{-1}), C=O bonds (around 1600 cm^{-1}), and C–O bonds (around 1020 cm^{-1}). The FTIR spectra of GEL and GEL-MA do not show major differences, both displaying stretching vibration bands of O–H and N–H bonds (around 3290 cm^{-1}), $\text{C}_{\text{sp}^2}\text{–H}$ bonds (at 3070 cm^{-1}), $\text{C}_{\text{sp}^3}\text{–H}$ bonds (at 2940 cm^{-1}), C=O bonds (around

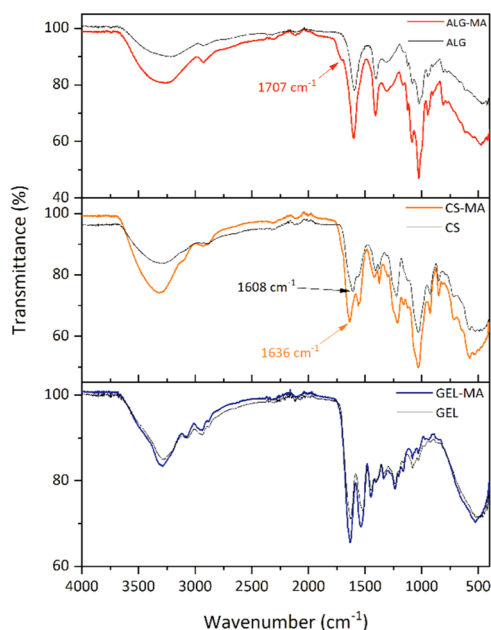


Figure 1. ATR-FTIR spectra of biopolymers before and after methacrylation.

1630 cm^{-1}), and C=C bonds (around 1530 cm^{-1}). The bands of MA groups in GEL-MA are likely overlapped with the intense signal of the GEL backbone bands.

The ^1H NMR analysis further confirmed functionalization of the biopolymers (Figure 2). The spectra of ALG-MA and CS-MA shows the characteristic doublets of vinyl protons at 5.75 and 6.14 ppm and multiplets of methylene protons at 3.39 and 3.55 ppm and methyl protons singlet at 1.94 ppm, corresponding to amidoethyl methacrylate functionalities. The ^1H NMR spectrum of GEL-MA shows peaks of vinyl protons of methacrylamide groups at 5.44 and 5.67 ppm, an additional doublet of vinyl protons at 5.75 and 6.14 ppm corresponding to methacrylate groups (secondary methacrylation reaction on hydroxy groups of GEL)⁴⁶ and the singlet of methyl protons at 1.94 ppm.

The degree of methacrylation of biopolymers was determined from the ^1H NMR spectra by the integration of the respective peaks affected by the chemical modification (for calculations details see Supporting Information). In ALG, the peak with a chemical shift of 5.04 ppm (Figure S1) corresponds to the hydrogen atoms bonded to anomeric carbons in the polysaccharide that is used as a reference to integrate. The changes of integration of the peak at 4.48 and 3.78 ppm (G5 and M5 peaks in Figure S1) allow the calculation of the degree of methacrylation respective to carboxylate groups (Figure S2). These peaks correspond to the hydrogen atoms bonded to the carbon atoms with carboxylate groups in ALG. The ^1H NMR spectrum of CS shown in Figure S3 displays the reference peak used for the degree of methacrylation calculation, corresponding to methyl protons of N-acetyl groups in sulfated galactosamine saccharide in the CS monomer. The degree of methacrylation in CS-MA is determined by the integral ratio of the methyl protons of the methacrylate groups (1.95 ppm) to the methyl protons of the N-acetyl groups (2.06 ppm) in the CS-MA spectrum of Figure 2. The degree of methacrylation of GEL-MA (relative to free amino groups) is determined by changes in the integral of the peak at 3.02 ppm. This peak corresponds to the methylene protons bonded to the carbon atoms with free amino groups in the lysine segments of GEL. The integral of the peaks at 7.29 and 7.37 ppm, corresponding to the aromatic protons of the phenylalanine segments, were used as the reference (Figure S5). Based on this methodology, the degrees of methacrylation were found to be 27% for ALG-MA, 50% for CS-MA, and 100% for GEL-MA, where the peak at 3.02 ppm is completely shifted and overlapped with the peak at 3.24 ppm and the peaks of free amino group protons disappear (Figure S6). These modified polymers were able to form a stable hydrogel by a test tube inversion method (Figure S7), after 5 min of irradiation with an UV lamp using a weight ratio of ALG-MA, CS-MA, and GEL-MA of 1:1:1 in the presence of a photoinitiator.

Characterization of GO. The chemical functionalities of synthesized GO were characterized by FTIR and UV-vis spectroscopy, whereas its microstructure was studied by XRD,

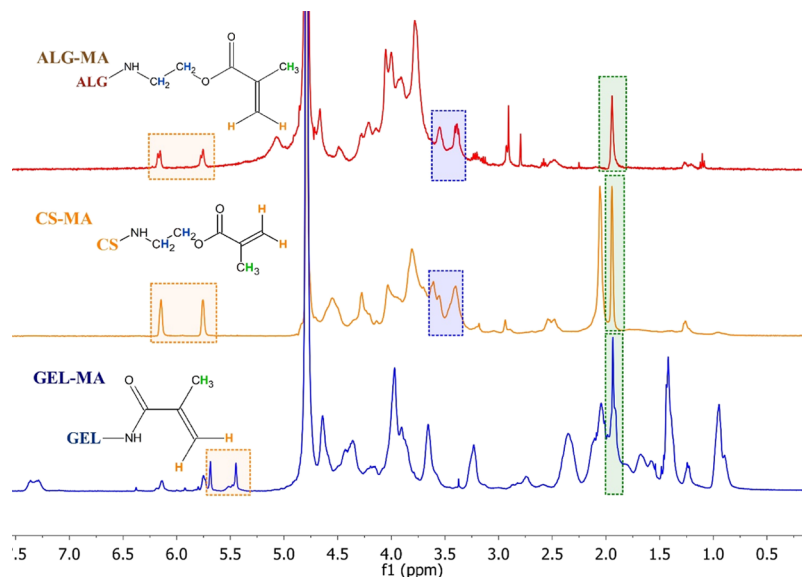


Figure 2. ^1H NMR spectra of methacrylated biopolymers. Characteristic peaks of MA moieties are highlighted in squares.

TEM, and POM. The FT-IR spectrum of GO (Figure 3a) displays a broadband around 3200 cm^{-1} , corresponding to the

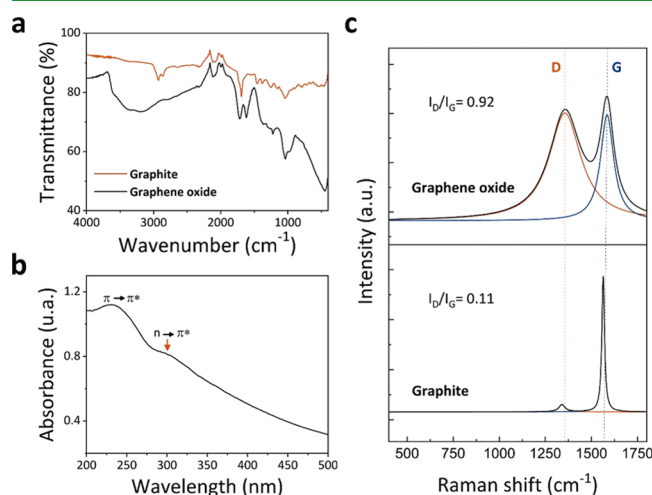


Figure 3. Spectroscopic characterization of synthesized GO: (a) ATR-FTIR spectra of GO (black line) and graphite precursor (red line). (b) UV-vis spectrum of GO measured on a water suspension 0.05 mg mL^{-1} . (c) Raman spectra of GO and graphite precursor where the D and G bands are indicated in red and blue, respectively, and its ratio of intensities are shown in the inset.

stretching vibrational mode of O–H bonds of the hydroxyl groups. The peaks associated with the stretching of C=O bonds of carbonyl groups, double bonds C=C from the aromatic carbon backbone, and C–O bonds from epoxy and hydroxyl groups are further observed at 1712 , 1618 , and 1040 cm^{-1} , respectively.

The UV-visible spectrum of a GO suspension in water shows a main peak around 230 nm corresponding to $\pi \rightarrow \pi^*$ electronic transitions in the aromatic basal plane and a shoulder around 300 nm consistent with $n \rightarrow \pi^*$ transitions due to oxygen atoms present in the functional groups (Figure 3b). Figure 3c displays the Raman spectra of GO and its graphite precursor, where the characteristic D band around 1357 cm^{-1} and G band around 1585 cm^{-1} were observed in the GO spectrum. The D band is attributed to defects produced after the oxidation of graphite, such as hydroxyl, epoxy, and carbonyl groups. The G band corresponds to a first-order scattering of the E_{2g} mode of the graphitic structure.⁴⁷ The intensity ratio between D and G peaks of the GO spectrum is ~ 8 -fold higher than graphite spectrum value, showing concordance with the structural modification due to the oxidation reaction.

Figure 4 displays the XRD patterns of graphite and GO showing that the oxidation and exfoliation process during GO synthesis produced an increment in the interlayer distance. While graphite presents an intense characteristic peak at 26.38° (2θ , layer distance $d = 0.34\text{ nm}$), GO exhibits a peak at 12.37° (2θ , $d = 0.71\text{ nm}$) corresponding to 001 plane reflections of few-layer GO. Residual graphitic structure peaks were not observed in GO by XRD. TEM images of synthesized GO confirmed the 2D layered sheet morphology (Figure 5a), and the analysis of FE-SEM images allowed the determination of the lateral size of GO sheets of $\sim 1\text{ }\mu\text{m}$ (Figure 5b). Based on these results, we conclude that the oxidation process of graphite was able to produce GO by adding oxygen-containing functional groups and disrupting the interlayer order.

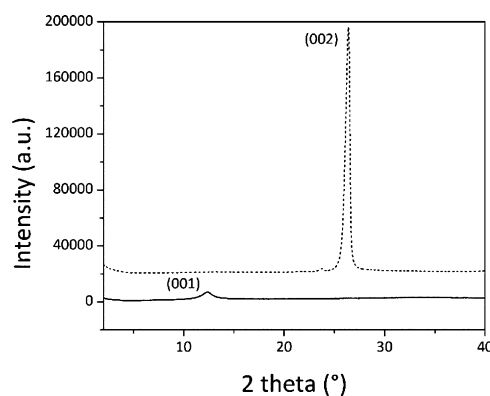


Figure 4. XRD powder diffractograms of GO (solid line) and graphite precursor (dotted line).

The liquid crystal (LC) property of GO in aqueous suspensions is an unexplored feature in tissue engineering, despite the high potential to template biomaterials.^{48,49} Figure 5c–f shows the LC nature of our GO by means of POM, where it is possible to observe a birefringent texture in an aqueous suspension having a concentration of $\sim 10\text{ mg mL}^{-1}$ of GO (Figure 5c,d) and in a wetted GO flake macroparticle (Figure 5e,f) when the samples are observed between crossed polarizer/analyzer (Figure 5d,f). The LC order of GO sheets in aqueous suspensions allows the obtention of anisotropic 2D flakes or papers and 1D annealing under determined conditions.⁵⁰

Scaffold Fabrication by 3D Printing. For the fabrication of hydrogel scaffolds using a 3D printing equipment, three ink formulations (ACG, ACG/GO0.1, and ACG/GO1 as detailed in Table 1) were used to study the effect of GO in this process. The weight proportion of methacrylated biopolymers (ALG-MA, CS-MA, and GEL-MA) in the ink was 1:1:1, with a concentration for each biopolymer of 6 mg mL^{-1} . This concentration and proportion was selected due to the printability of the inks in our 3D printer, and previous results indicating that in binary ALG-GEL systems this ratio ($\sim 1:1$) showed enhanced cell adhesion and proliferation.^{10,11,24} Moreover, under these conditions, the CS proportion relative to ALG and other bioconjugated hydrogels is in the chondroinductive range (25 – 75%).^{19–21,24} Pure ALG was further added to each ink formulation because methacrylation in ALG-MA reduces the amount of crosslinkable sites, and consequently, the ionic crosslinking with calcium(II) is less efficient.⁵¹

By employing Materialise Magics software, a scaffold of $30 \times 30 \times 1\text{ mm}^3$ (length \times width \times height) was drawn, and the obtained STL file was processed with Perfactory Software Suite in order to divide the designed structure into four layers. Finally, a mesh-like inner pattern with 1.5 mm of thread spacing was set with Visual Machine software from the 3D Bioplotter. Because of the heterogeneity (molecular weight and chemical composition) of the biopolymers, both the polymer concentration and the printing parameters had to be optimized according to the printing tests.

Video S1 shows the 3D printing process of ACG/GO0.1, ink at 5°C during the micro-extrusion from the cartridge on a Petri dish having a CaCl_2 100 mM solution at 2°C . First, ALG and GEL chains presented ionic and thermotropic gelation processes, respectively. When a few layers are printed, more CaCl_2 solution is added to ensure the crosslinking of

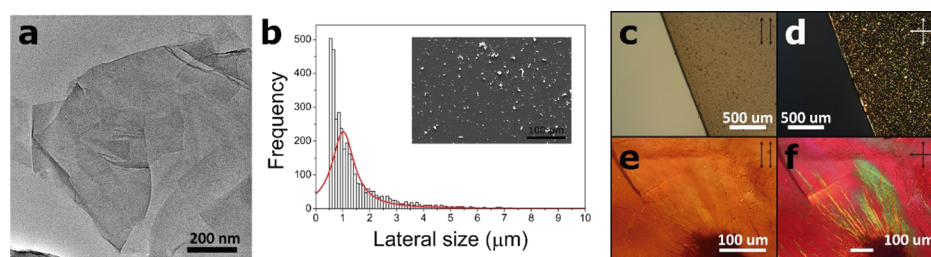


Figure 5. Microscopic analysis of GO. (a) TEM microphotography of few-layer GO sheets. (b) Lateral size distribution of GO particles. (c) Liquid crystalline properties of an aqueous suspension of GO observed with a parallel polarizer/analyzer and (d) crossed polarizer/analyzer filters. The LC order is maintained in a wetted flake of GO, which is observed in (e) parallel polarizer/analyzer and (f) crossed polarizer/analyzer (with a retardation plate) filters.

Table 1. Composition of Hydrogel Inks (mg mL^{-1})

	ACG	ACG/GO0.1	ACG/GO1
ALG	10	10	10
ALG-MA	6	6	6
CS-MA	6	6	6
GEL-MA	6	6	6
GO	0	0.1	1
PI ^a	0.5	0.5	0.5

^aPhotoinitiator.

ALG and ALG-MA. The 3D printed scaffolds are then irradiated with UV light for secondary photocrosslinking and washed afterward with deionized water and freeze-dried. Figure 6a–c displays digital pictures of the lyophilized 3D printed scaffolds using the three ink formulations. Under the same printing conditions (optimized for the performance with ACG ink meaning a printing speed = 50 mm s^{-1} , extrusion pressure = 1 bar, and 25 G needle tip), the scaffolds printed with inks containing GO show a noticeable higher shape fidelity and spatial resolution than ink without GO. FE-SEM image analysis shows a flattening of the thread in the scaffolds having GO after the freeze-drying process (Figure 6e,f). The

morphologic analysis of the surface on strands show an increment in the roughness when GO is added (Figure 6g–i). While a smooth surface is observed in the scaffold with ACG composition, fibrillar and bumped micro-topography are observed on the surface of 3D printed scaffolds using ACG/GO01 and ACG/GO1 inks, respectively.

The anisotropy features in the threads of 3D printed scaffolds were studied by POM. The as-printed strands and the corresponding freeze-dried/rehydrated threads of the scaffolds without GO (ACG) did not show significant birefringence (Figure S8a–c), indicating the isotropic nature of these threads. Scaffolds with a low GO concentration (ACG/GO01) did not also show significant birefringence in the as-printed threads (Figure S8e), although a weak birefringence with a grooved shape was observed on the threads after the freeze-drying/rehydration process, in accordance with the microfibril topography observed in the Figure 6h. This result is indicative of partly ordered and localized anisotropy along the ACG/GO01 threads (Figure S8f). Figure 7 shows POM images of a 3D printed thread produced using ACG/GO1 ink. Depending on the directional angle of the thread, it exhibits intense birefringence with red or blue color interference when the sample is observed with a crossed polarizer/analyzer and a

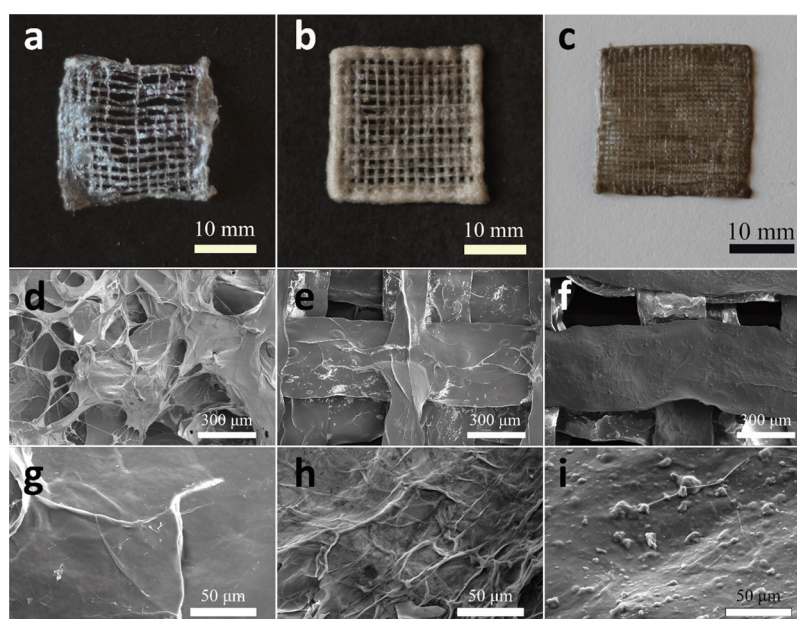


Figure 6. Full-size appearance of lyophilized scaffolds 3D printed with (a) ACG, (b) ACG/GO0.1, and (c) ACG/GO1 inks. FE-SEM images of thread surfaces: (d,g) ACG, (e,h) ACG/GO0.1, and (f,i) ACG/GO1 3D printed scaffolds.

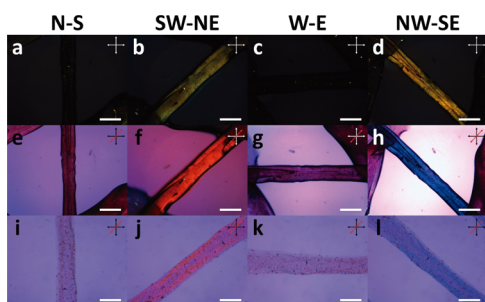


Figure 7. POM images of anisotropic threads of scaffolds 3D printed with ACG/GO1 ink. (a–d) POM images of an as-printed thread observed with different angles between crossed polarizer/analyzer filters, (e–h) as-printed thread observed with a retardation plate between crossed polarizer/analyzer filters and (i–l) rehydrated thread after the freeze-drying process, observed with a retardation plate between crossed polarizer/analyzer filters. Scale bar: 400 μm , N–S: North–South, SW–NE: Southwest–Northeast, W–E: West–East, and NW–SE: Northwest–Southeast directions.

first-order (λ) retardation plate. While the thread does not exhibit birefringence at 0° and 90° with respect to the polarizer (N–S and W–E columns in Figure 7), the thread acquires a first-order red color (fast axis) when the thread orientation is Southwest–Northeast (SW–NE, Figure 7f,j) and a second-order blue color (slow axis) when the thread orientation is Northwest–Southeast (NW–SE, Figure 7h,i). The homogeneous birefringence in the thread indicates an anisotropic molecular order along the major axis. This order was observed for threads printed with ACG/GO1 in both the as-printed (Figure 7a–h) and after freeze-drying/rehydration process (Figure 7i–l), and differences were not observed in the thread after (only ionocrosslinking) and before photocrosslinking (as-printed). Compounds with LC mesophases can yield this kind of anisotropic microfibers⁵² or induce the alignment of polymeric chains during the fiber fabrication process.⁵³ Aqueous GO suspensions have exhibited a stable lyotropic nematic mesophase (with a volume fraction of 100%) in concentrations higher than 8 mg mL^{-1} .⁵⁴ Below this critical concentration, the isotropic and nematic phases co-exists, showing only $\sim 3\%$ of nematic mesophase at GO concentration of 1 mg mL^{-1} . However, when a GO suspension at low concentration (for instance $< 1 \text{ mg mL}^{-1}$) passes through a tube at high velocity, such as the needle of a 3D printer, the GO sheets can exhibit alignment induced by the flow.⁵⁵ Furthermore, recent studies show that lyotropic LC properties of GO are stabilized, and the critical concentration of mesophase formation is lowered, by the influence of ALG in

composites.⁵⁶ For this reason, it is likely that the micro-extrusion process and the LC mesophase of GO trigger a preferential molecular orientation along the 3D printed threads. Anisotropic structures such as fibers and films are naturally found in the body tissue, and for this reason, biomimetic anisotropic scaffolds for muscle, neural, and tendon tissues have attracted attention.⁵⁷ In recent years, some tissue engineering research have focused their work on the development of anisotropic scaffolds by an LC template to mimic the natural environment and architecture of the tissue.⁵⁸ Therefore, GO appears as a novel filler triggering anisotropic behavior in biopolymer composites.

Water Content and Swelling Ratio of Scaffolds. The water content of photocrosslinked scaffolds and water uptake capacity after lyophilization was studied for three compositions (ACG, ACG/GO01, and ACG/GO1). Figure 8a displays the water mass fraction of as-photocrosslinked and freeze-dried/rehydrated scaffolds. The as-photocrosslinked scaffolds exhibit high water mass fraction (~ 0.96), and no differences between the three samples was observed. When the scaffolds are rehydrated after lyophilization, the water content in scaffolds decrease between 6 and 10%, and the water absorption capacity in nanocomposite scaffolds is significantly superior to ACG scaffolds. Furthermore, the swelling ratio of GO-containing scaffolds are between 50 and 66% higher than ACG scaffolds, being able to increase their mass up to 10-fold by absorbing water (Figure 8b). These results suggest that the incorporation of GO into the biopolymeric network increases the hydrophilicity and water retention, probably due to the presence of polar oxygen-rich functional groups that could interact with water molecules by hydrogen bonding.

Rheological Properties of Inks. The rheological behavior of ink formulations used for 3D printing scaffold fabrication was studied at 4°C . The pure hydrogel matrix and the composites presented a similar viscosity with a shear thinning behavior during the whole range of applied shear rates (Figure 9a). Despite the low concentration of GO used, the nanocomposites displayed lower viscosities than the pure hydrogel, which is likely associated with the reduction of the polymer free volume⁵⁹ or the adsorption of polymer molecules on the particle surface.⁶⁰ Figure 9b shows the storage and the loss moduli as a function of frequency for the three ink formulations. All inks exhibit liquid-like hydrogel behaviors before crosslinking with low modulus values (between 10 and 100 Pa) and $\tan \delta = G''/G' > 1$. The data of the storage and the loss moduli fit with a Maxwell scaling law; this means that at low frequencies ($\omega \rightarrow 0$), $G' \approx \omega^2$ with a slope = 1 and $G'' \approx \omega$ with a slope = 2. After the addition of a calcium chloride

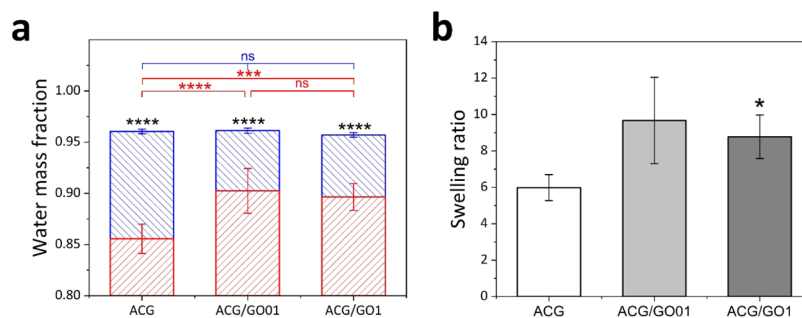


Figure 8. Water content in the scaffolds: (a) water mass fraction in scaffolds after photocrosslinking (blue bars) and after the freeze-drying/rehydration process (red bars). (b) Swelling ratio of scaffolds. ns: not significant, *: $p < 0.05$, ***: $p < 0.001$, and ****: $p < 0.0001$.

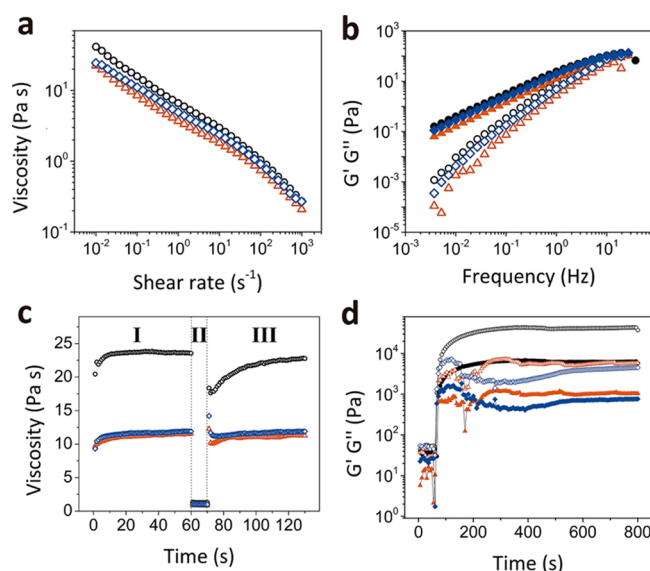


Figure 9. Rheological characterization of ACG (black circles), ACG/GO0.1 (red triangles), and ACG/GO1 (blue rhombus) inks. (a) Flow curves of the different ink formulations. (b) Storage modulus, G' (open symbols) and loss modulus, G'' (closed symbols) of the ink formulations as a function of the frequency. (c) Shear thinning and recovery behavior of hydrogels simulating the printing process by the rheological study: stage I, before printing; stage II, during printing; and stage III, after printing. (d) Storage modulus, G' (open symbols) and loss modulus, G'' (closed symbols) measured over 800 s where 100 mM CaCl_2 solution was added 60 s after the measurement was started.

solution ($t = 60$ s), a clear transition to solid-like characteristics is observed with a drastic increase in the moduli of several orders of magnitude, while G' crosses G'' ($\tan \delta < 1$), as displayed in the kinetic curves of ionotropic crosslinking (Figure 9d). Figure 9c shows the thixotropy study made in order to mimic the shear rate effect on the viscosity of inks during the 3D printing process.⁶¹ The first 60 s at a low shear rate of 0.1 s^{-1} (stage I) represents the inks in cartridges, followed by a short increment of high shear rates (100 s^{-1} for 10 s) in stage II, which mimics the flow of the inks through the needle, and the last 60 s at 0.1 s^{-1} displays the viscosity recovery of hydrogels after the extrusion process (stage III). The inks containing GO exhibit both a lower decrease in the viscosity during stage II and lower recovery times than ACG ink. Because the viscosity of the inks is similar, this does not seem to have a significant effect on the printability. The

thixotropic property of the hydrogels is an important factor in the printability and resolution of the 3D printed scaffolds as the required time to recover the initial viscosity of the ink relates directly with the printed strand fidelity (width).^{45,62} Rheological studies show that ACG ink presents high recovery times (64 s to reach the 97% of the initial viscosity value in stage I), and therefore the threads can be segmented or merged with neighboring threads. In contrast, ACG/GO0.1 and ACG/GO1 inks take only 12 and 1 s, respectively, to recover the 97% of initial viscosity, allowing the extrusion of thinner and well-defined threads. This process is relevant as it relates with the stability of the strands until the addition of the ionotropic crosslinker. The GO sheets can interact with the biopolymeric chains through hydrogen bonding, where GO acts as a physical crosslinker that improves the viscosity recovery time.⁴⁵

Mechanical Properties of Hydrogels. The effect of GO on the mechanical properties of scaffolds was studied by means of uniaxial unconfined compression tests. The averaged stress–strain curves for three kinds of scaffolds are shown in Figure 10a. The profile of the ACG/GO01 curve (red line) does not differ considerably from ACG (black line); therefore, there is no mechanical reinforcement attributable to GO because of the low concentration in this formulation. The scaffold with higher GO concentration (ACG/GO1, blue line curve) exhibits improved mechanical strength compared to ACG. The compressive elastic moduli of scaffolds quantify the superior mechanical performance of ACG/GO1 scaffolds (Figure 10b). The compressive modulus in ACG/GO1 is $\sim 60\%$ higher than hydrogels without and with a low concentration of GO. The ACG and ACG/GO01 compressive moduli did not show significant differences. The increase in the compressive elastic modulus can be attributed to the improved mechanical behavior of the GO nanofiller further forming bridges that reinforces the three-dimensional structure of the hydrogel scaffolds.³¹

Biological Interaction of Scaffolds with hADMSCs.

The viability of hADMSCs on 3D printed scaffolds was evaluated by alamarBlue and Live/Dead fluorescence staining assay. For alamarBlue assay, hADMSCs (passage 9) were seeded on the 3D printed scaffolds, utilizing pure ALG scaffold as a control. Figure 11a shows the evolution of the hADMSC proliferation (displayed as mean fluorescence intensity) on 3D scaffolds during 14 days. The average cell viability in each scaffold is not significantly different from controls (at the 0.05 level) during the first 3 days, suggesting that the chemical composition of the different inks is cytocompatible with hADMSCs at an early stage, independent of the bioconjugation.

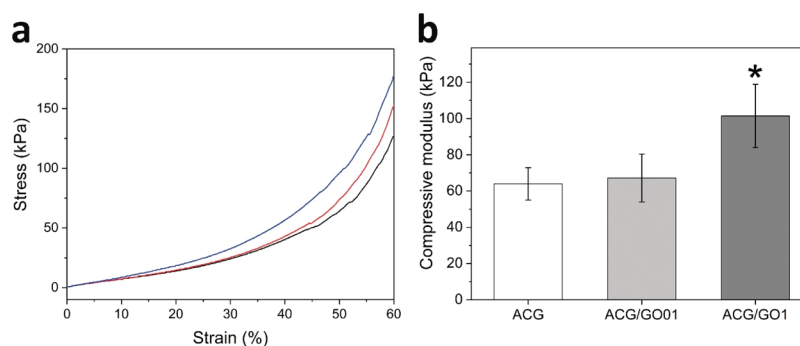


Figure 10. Effect of GO incorporation on mechanical properties of scaffolds. (a) Averaged stress–strain curves of ACG (black line), ACG/GO01 (red line), and ACG/GO1 (blue line) hydrogels. (b) Compressive elastic moduli of scaffolds (*: $p < 0.05$).

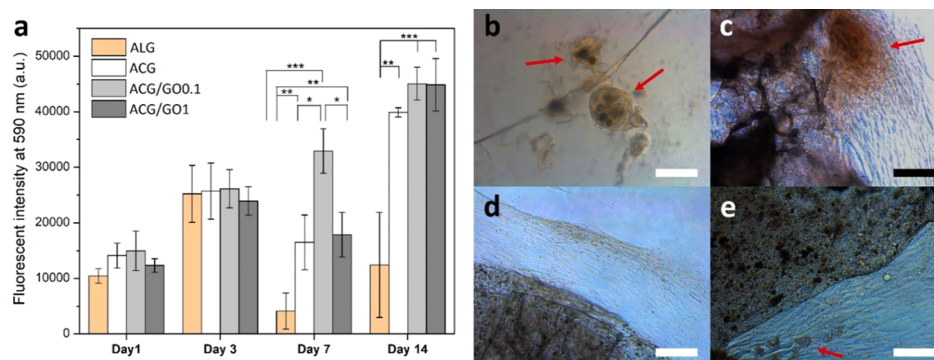


Figure 11. Proliferation of hADMSCs on 3D printed scaffolds. (a) Cell proliferation quantification by alamarBlue assay (*: $p < 0.05$, **: $p < 0.01$ and ***: $p < 0.001$). Contrast phase microphotography of cell-seeded scaffolds at day 7: (b) ALG, (c) ACG, (d) ACG/GO0.1, and (e) ACG/GO1. Cell aggregates are denoted with arrows (scale bar: 100 μm).

tion and the presence of GO. However, after one week, the proliferation of hADMSCs on bioconjugated scaffolds was significantly superior as compared with pure ALG control scaffolds, as the cell amount decreases considerably on the latter. Notably, ACG/GO0.1 scaffolds presented higher cell proliferation than ACG and ACG/GO1 scaffolds. The low cell viability in ALG scaffolds can be explained by cell aggregation, as shown in Figure 11b, meaning that in these scaffolds the cell–cell interaction is preferred rather than the cell–material interaction.⁶³ These cellular aggregates can be detached from the scaffolds during both the successive culture media changes through aspiration and the washing procedure of the assay, which causes a dramatic decrease in the cell number. The cell proliferation on the scaffolds increases significantly, when ALG bioconjugates with CS and GEL. This increment in proliferation means that the cells prefer to attach on the scaffold surface rather than to other cells. Notably, in the ACG/GO0.1 scaffolds, the cells proliferate homogeneously on the surface and around the threads of the scaffold without the formation of cell aggregates (Figure 11d). By adding more GO, the high proliferation produced not only cells distributed on the scaffold surface but also small cell aggregates (Figure 11e). After 14 days, the cultured cells reached a maturation state with a higher cell number compared to day 7. Probably, the production of ECM by the cells increases their adhesion on the bioconjugated scaffolds. Particularly, the GO-containing bioconjugated scaffolds exhibited significantly higher hADMSC proliferation, showing up to 3.6-fold higher fluorescence intensity as compared with pure ALG scaffolds and as compared with the same samples at day 1 of culture. These results confirm the effectiveness of GEL as a bioconjugant agent for the improvement of cell adhesion on scaffolds.

The survival of adhered hADMSCs on 3D printed scaffolds was studied by Live/Dead assay with calcein-AM/propidium iodide staining and fluorescence microscopy. Figure 12 shows representative fluorescence microscopy images of the three different scaffolds seeded with hADMSCs (passage 6) at day 7. The results show the survival of all adhered hADMSCs (green cells) on the scaffolds regardless of the formulation of the ink used to print it. This result suggests that the decrease of fluorescence intensity in alamarBlue assay for ACG and ACG/GO1 at day 7 (Figure 11a) could be due to cell aggregation and subsequent detachment or cell metabolism inhibition, rather than cell dead due to the cytotoxic effect of materials. The presence of GO did not produce a cytotoxic effect on

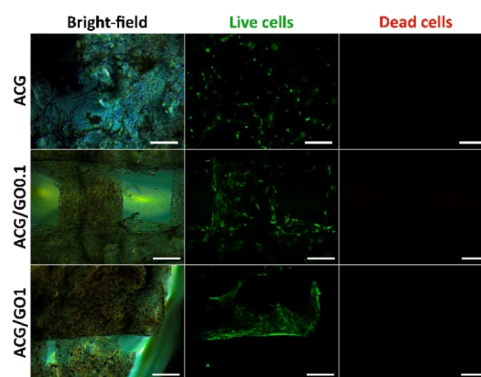


Figure 12. Representative fluorescence microscopy images of Live/Dead assay of hADMSCs seeded on 3D printed scaffolds at day 7 (scale bar: 200 μm).

hADMSCs during the studied time. The cytotoxic level of pure GO on hMSCs can be found at concentrations ranging from 10 to 100 $\mu\text{g mL}^{-1}$.⁶⁴ However, our results are in accordance with previous reports of cytocompatible nanocomposites having GO with higher concentrations that have shown improved cell adhesion, proliferation, and differentiation of hMSCs for tissue engineering applications.⁶⁵ This behavior can be explained through the interaction of GO with the polymer network by hydrogen bonding, allowing a slow release of GO to the culture medium, which reduces its cytotoxicity.⁶⁶ Furthermore, GO is able to adsorb proteins of biological surrounding through hydrophobic, hydrophilic, and π – π interactions which improve cell migration, distribution, and attachment to the scaffold.⁶⁷ Motivated by the potential toxicity of GO, its release from nanocomposite scaffolds over 28 days in PBS at 37° C was studied. The results showed a low release of GO for both ACG/GO01 and ACG/GO1 samples, with a cumulative GO release between 6 and 10 $\mu\text{g mL}^{-1}$ at day 28 (Figure S9). These results do not consider the frequent changes of the culture medium, which would expose the cells to a lower effective GO concentration. For this reason, the levels of free GO released from nanocomposite scaffolds can be considered safe for the hADMSCs.

Figure 13 shows representative images of the adhered hADMSCs (passage 4) on scaffolds printed with ACG (a,b), ACG/GO0.1 (c,d), and ACG/GO1 (e,f) at day 7. The F-actin filaments of the cell cytoskeleton and cell nuclei were stained with FITC-phalloidin (green) and DAPI (blue), respectively. Figure 13 confirms the observation by contrast phase

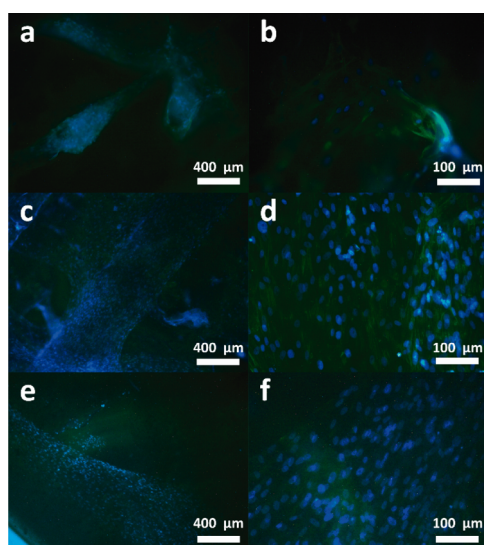


Figure 13. Fluorescence microscopy images of hADMSCs seeded on 3D printed scaffolds at day 7. Cytoskeleton F-actin (green) and nuclei (blue) of hADMSCs are shown for (a,b) ACG, (c,d) ACG/GO0.1, and (e,f) ACG/GO1 scaffolds.

microscopy (Figure 11) as the hADMSCs on the ACG scaffold tended to form cell aggregates and a nonuniform distribution on the scaffold (Figure 13a), whereas hADMSCs seeded on GO-containing scaffolds showed higher cell proliferation with a more homogeneous distribution. Particularly, the ACG/GO0.1 scaffold (Figure 13c,d) displayed uniformly distributed hADMSCs with a high cell density along the printed threads. The well-defined mesh-like thread pattern in the GO-containing 3D printed scaffolds could help to obtain a more ordered cellular distribution. Regarding the stability of scaffolds, the macrostructure showed full integrity after 35 days of culture with hADMSCs in the physiological condition of pH and temperature, as displayed on the stereomicroscopy

study (Figure S10). All the scaffolds (independent of composition) maintained its original shapes during the formation and maturation of a new tissue. Photocrosslinking of methacrylated biopolymers and ionotropic crosslinking of ALG segments likely help to retain the structural integrity during the time needed for the growth of new tissue.

Motivated by the anisotropic molecular order along the thread major axis (Figure 7), the directionality of hADMSCs adhered to 3D printed scaffolds was studied by image analysis from TRITC-phalloidin stained microphotography after 28 days of culture in CCM. Figure 14 shows the cytoskeleton staining of hADMSCs (top) and its respective frequency distribution of cell directionality histograms (bottom) for each scaffold composition. In scaffold ACG, the cells are randomly oriented without a marked angular direction of preference (Figure 14a). The addition of GO considerably increases the directionality on the cell proliferation, likely due to the anisotropic structure of the 3D printed threads (Figure 14b,c). This result offers a novel platform for biomaterial-guided cell organization where anisotropic structures are required, such as tendons and muscle fibers.^{57,68}

Chondrogenesis Studies. Chondrogenic differentiation of hADMSCs was analyzed by immunofluorescence staining of chondrogenic markers for collagen type II, aggrecan, and SOX 9. Figure 15 shows stereomicroscopic fluorescence images of immunofluorescence (green) and F actin (red) staining for the 3D printed scaffolds after 28 days of culture in a conditioned (chondrogenic agents-free) culture medium. Positive expression of collagen type II, aggrecan, and SOX 9 was found in the three scaffolds (with and without GO), suggesting that the biopolymeric matrix based on bioconjugated ALG with both GEL and CS induces chondrogenic differentiation on hADMSCs. Scaffolds without primary/secondary antibody incubation served as negative controls (Figure S10).

High-density cell aggregates in the scaffolds without GO and with high GO concentration (ACG and ACG/GO1 respectively) were observed. Compared with images after 7

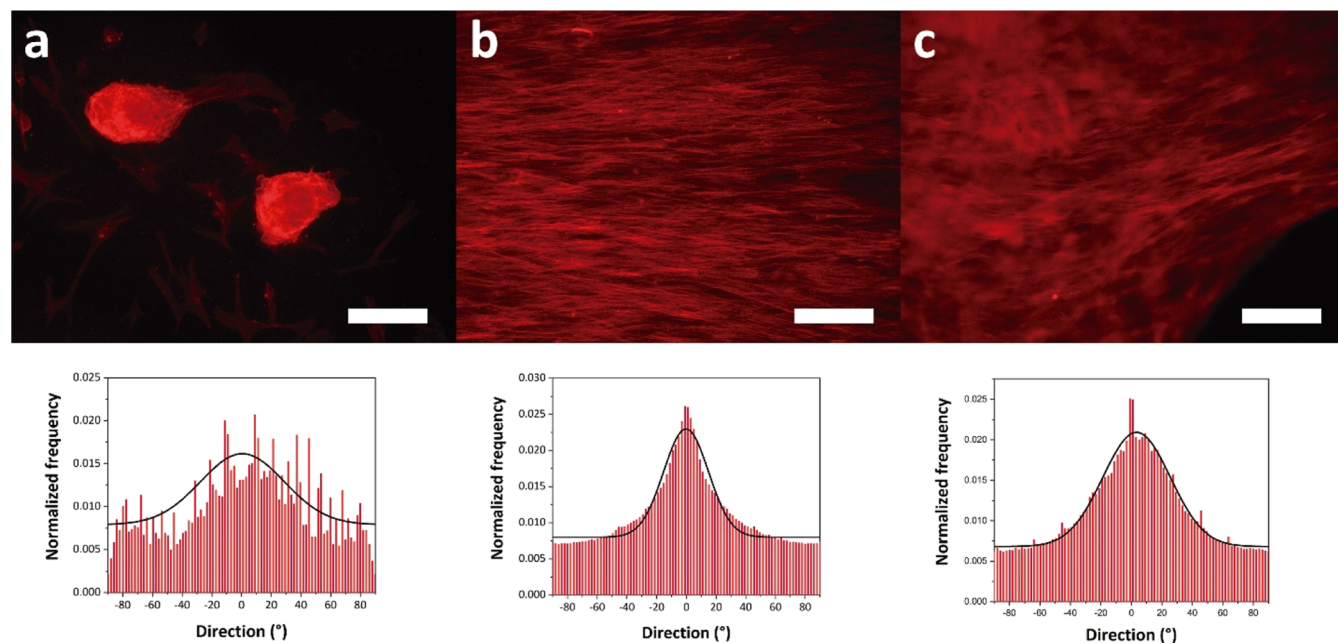


Figure 14. Fluorescence microphotographs of cytoskeleton F actin (top) and its respective frequency distributions of cell directionality histograms, where 0° correspond to the thread direction (bottom) for (a) ACG, (b) ACG/GO0.1, and (c) ACG/GO1 3D printed scaffolds.

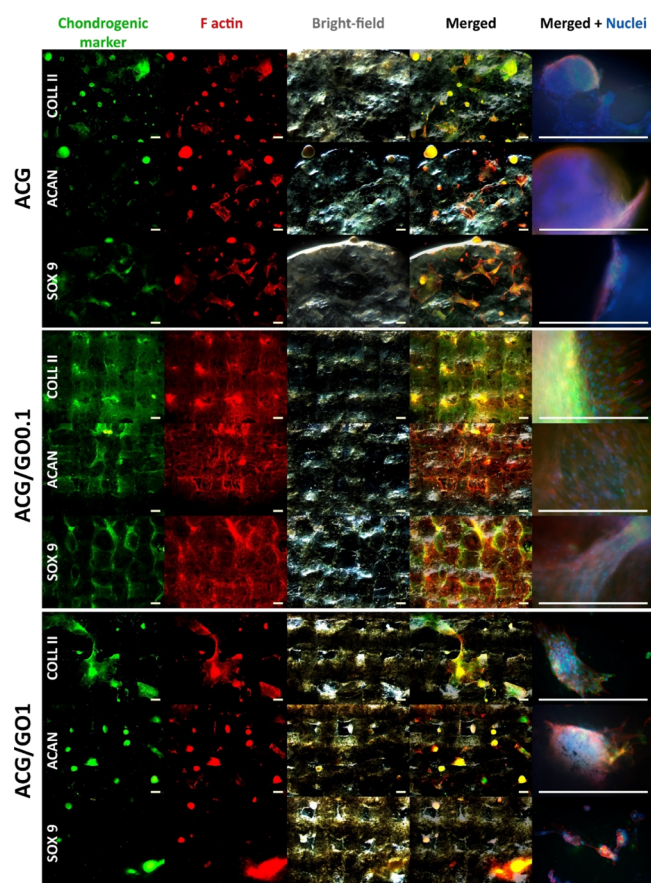


Figure 15. Fluorescence images of immunostaining for chondrogenic markers (green) collagen type II (COLL II), aggrecan (ACAN), and SOX 9 for the 3D printed scaffolds: ACG (top), ACG/GO0.1 (middle), and ACG/GO1 (bottom), after 28 days of culture. Cytoskeleton F actin and nuclei counter staining are shown in red and blue, respectively (scale bar: 500 μm).

days (Figure 13), cells on ACG/GO1 tend to form aggregates after 28 days of culture. In contrast, the presence of GO at low concentration (ACG/GO0.1) improves notably the long-term cell distribution and ECM deposition on the 3D printed scaffold, exhibiting a homogeneous cell proliferation on the scaffold thread, porous, and around the scaffold edge. This behavior could be explained by the micro-topography on the thread surface, while the anisotropic grooved surface of ACG/GO01 helps increase and guides the adhesion of cells; the smoother surface on ACG/GO1 (Figure 6i) could promote the long-term cell–cell interaction rather than the cell–biomaterial interaction, producing cell aggregation. Otherwise, the formation of cell aggregates is a common phenomenon in the chondrogenesis process and has already been reported in CS-based scaffolds.⁶⁹ This phenomenon was mainly observed in ACG and ACG/GO1 scaffolds but was completely diminished in the ACG/GO01 scaffolds showing uniformity in the formation of a new tissue (middle in Figure 15).

In a recent study, Shen et al. evaluated the effect of GO nanocomposite hydrogels in exogenous TGF β -free chondrogenesis of hMSCs.³⁶ This pioneer work evidenced the chondroinductive property of GO and suggests that GO is able to concentrate locally pro-chondrogenic biomolecules in the cellular environment. A chondrogenic culture medium supplemented with pro-chondrogenesis agents [insulin–transferrin–selenium (ITS), dexamethasone, L-ascorbic acid 2-

phosphate, and L-proline] was used in that study; however, our study shows the intrinsic chondroinductive effect of the developed biomaterials without the need of any exogenous pro-chondrogenic factor in the culture medium. The secretion of collagen type II after 28 days in ACG/GO0.1 scaffolds shows high similarity in density and anisotropic distribution (detailed immunofluorescence image in Figure S11) with the observed immunofluorescent analysis of the human cartilage tissue and tissue-engineered neocartilage.⁷⁰ The results suggest that ACG/GO0.1 scaffolds have the optimal properties for printability, biocompatibility, cell proliferation, and interconnected neocartilage ECM deposition, where the biopolymer matrix and GO acts synergistically in the hADMSC chondrogenic differentiation.

CONCLUSIONS

In this work we present novel bioconjugated nanocomposite hydrogels based on ALG, crosslinked with GEL and CS, and GO particles as inks for 3D printing scaffolds. The incorporation of GO into the ink formulation enhanced its printability, obtaining scaffolds with higher shape fidelity and resolution than ink without GO, due to an enhanced thixotropic behavior. Threads printed with ACG/GO1 result in anisotropic fibers, probably induced by liquid crystalline properties of GO, with interesting projections for tissue engineering where cellular alignment is required. 3D printed bioconjugated scaffolds showed to be cytocompatible with hADMSCs and samples with GO presented outstanding cell proliferation, alignment, and distribution in the scaffolds. Immunostaining analysis indicated that the bioconjugated ALG polymer matrix is intrinsically chondroinductive on hADMSC differentiation after four weeks culture in the nonchondrogenic medium. The superior biocompatibility and bioactivity of the 3D printed scaffolds based on our bioconjugated nanocomposite with hADMSCs make them as candidates for cartilage tissue engineering.

ASSOCIATED CONTENT

Supporting Information

The Supporting Information is available free of charge at <https://pubs.acs.org/doi/10.1021/acsami.9b22062>.

¹H NMR characterization of used pure commercial biopolymers and degree of methacrylation determination for ALG-MA, CS-MA, and GEL-MA, photocrosslinking test, cumulative GO release, negative control images for anisotropy and immunofluorescence studies, stereomicroscopy images of scaffolds after 35 days, and immunofluorescence image of anisotropic cell organization of neocartilage in ACG/GO01 scaffold (PDF)

Video showing the 3D printing process (ZIP)

AUTHOR INFORMATION

Corresponding Authors

Felipe Olate-Moya – Universidad de Chile, Santiago, Chile; orcid.org/0000-0002-2000-0708; Email: felipe.olate@ing.uchile.cl

Humberto Palza – Universidad de Chile, Santiago, Chile, and Millennium Nuclei in Soft Smart Mechanical Metamaterials, Santiago, Chile; orcid.org/0000-0001-

5246-6791; Phone: +56229780795; Email: hpalza@ing.uchile.cl

Other Authors

Lukas Arens – Karlsruhe Institute of Technology (KIT), Karlsruhe, Germany

Manfred Wilhelm – Karlsruhe Institute of Technology (KIT), Karlsruhe, Germany; orcid.org/0000-0003-2105-6946

Miguel Angel Mateos-Timoneda – The Barcelona Institute of Science and Technology, Barcelona, Spain, CIBER en Bioingeniería, Biomateriales y Nanomedicina (CIBER-BBN), Madrid, Spain, and Technical University of Catalonia (UPC), Barcelona, Spain; orcid.org/0000-0001-7657-1414

Elisabeth Engel – The Barcelona Institute of Science and Technology, Barcelona, Spain, CIBER en Bioingeniería, Biomateriales y Nanomedicina (CIBER-BBN), Madrid, Spain, and Technical University of Catalonia (UPC), Barcelona, Spain; orcid.org/0000-0003-4855-8874

Complete contact information is available at: <https://pubs.acs.org/10.1021/acsami.9b22062>

Author Contributions

The manuscript was written through contributions of all authors. All authors have given approval to the final version of the manuscript.

Notes

The authors declare no competing financial interest.

ACKNOWLEDGMENTS

The authors thank the financial support of CONICYT under FONDECYT Project 1150130, FONDEQUIP Projects EQM150101, EQM170103 and EQM140012, and funding from Millennium Science Initiative of the Ministry of Economy, Development and Tourism, grant “Nuclei for Soft Smart Mechanical Metamaterials”. F.O.-M. thanks to CONICYT Beca de Doctorado Nacional 21150039.

ABBREVIATIONS

AEMA, 2-aminoethyl methacrylate hydrochloride
 ALG, alginate
 ALG-MA, alginate methacrylated
 ATR–FTIR, attenuated total reflection Fourier transform infrared spectroscopy
 CCM, conditioned culture medium
 CS, chondroitin sulfate
 CS-MA, chondroitin sulfate methacrylated
 DAPI, 4',6-diamidino-2-phenylindole
 ECM, extracellular matrix
 EDC, *N*-(3-dimethylaminopropyl)-*N'*-ethylcarbodiimide hydrochloride
 FBS, fetal bovine serum
 FE-SEM, field emission scanning electron microscopy
 FITC, fluorescein isothiocyanate
 GAG, glycosaminoglycan
 GEL, gelatin
 GEL-MA, methacryloyl gelatin
 Gly, glycine
 GO, graphene oxide

hADMSC, human adipose tissue-derived mesenchymal stem cell
 hMSC, human mesenchymal stem cell
¹H NMR, proton nuclear magnetic resonance
 LVR, linear viscoelastic region
 MAA, methacrylic anhydride
 MEM α , minimum essential medium alpha
 MWCO, molecular weight cut-off
 MES, 2-(*N*-morpholino)ethanesulfonic acid
 NHS, *N*-hydroxysuccinimide
 PI, 2-hydroxy-4'-(2-hydroxyethoxy)-2-methylpropionone photoinitiator
 PBS, phosphate buffered saline
 PG, proteoglycan
 POM, polarized light microscopy
 RGD, arginylglycylaspartic acid
 STL, standard triangle language
 TEM, transmission electron microscopy
 TRITC, tetramethylrhodamine
 UV–vis, ultraviolet–visible spectroscopy
 XRD, X-ray diffraction

REFERENCES

- (1) Zhu, W.; Ma, X.; Gou, M.; Mei, D.; Zhang, K.; Chen, S. 3D Printing of Functional Biomaterials for Tissue Engineering. *Curr. Opin. Biotechnol.* **2016**, *40*, 103–112.
- (2) Bose, S.; Vahabzadeh, S.; Bandyopadhyay, A. Bone Tissue Engineering Using 3D Printing. *Mater. Today* **2013**, *16*, 496–504.
- (3) Stoppel, W. L.; Ghezzi, C. E.; McNamara, S. L.; Black, L. D., III; Kaplan, D. L. Clinical Applications of Naturally Derived Biopolymer-Based Scaffolds for Regenerative Medicine. *Ann. Biomed. Eng.* **2015**, *43*, 657–680.
- (4) Balakrishnan, B.; Banerjee, R. Biopolymer-Based Hydrogels for Cartilage Tissue Engineering. *Chem. Rev.* **2011**, *111*, 4453–4474.
- (5) Vicini, S.; Mauri, M.; Wichert, J.; Castellano, M. Alginate Gelling Process: Use of Bivalent Ions Rich Microspheres. *Polym. Eng. Sci.* **2017**, *57*, 531–536.
- (6) Jang, J.; Park, J. Y.; Gao, G.; Cho, D.-W. Biomaterials-Based 3D Cell Printing for next-Generation Therapeutics and Diagnostics. *Biomaterials* **2018**, *156*, 88–106.
- (7) Huang, G.; Li, F.; Zhao, X.; Ma, Y.; Li, Y.; Lin, M.; Jin, G.; Lu, T. J.; Genin, G. M.; Xu, F. Functional and Biomimetic Materials for Engineering of the Three-Dimensional Cell Microenvironment. *Chem. Rev.* **2017**, *117*, 12764–12850.
- (8) McBeth, C.; Lauer, J.; Ottersbach, M.; Campbell, J.; Sharon, A.; Sauer-Budge, A. F. 3D Bioprinting of GelMA Scaffolds Triggers Mineral Deposition by Primary Human Osteoblasts. *Biofabrication* **2017**, *9*, 015009.
- (9) Dong, Y.; Sigen, A.; Rodrigues, M.; Li, X.; Kwon, S. H.; Kosaric, N.; Khong, S.; Gao, Y.; Wang, W.; Gurtner, G. C. Injectable and Tunable Gelatin Hydrogels Enhance Stem Cell Retention and Improve Cutaneous Wound Healing. *Adv. Funct. Mater.* **2017**, *27*, 1606619.
- (10) Yao, R.; Zhang, R.; Luan, J.; Lin, F. Alginate and Alginate/Gelatin Microspheres for Human Adipose-Derived Stem Cell Encapsulation and Differentiation. *Biofabrication* **2012**, *4*, 025007.
- (11) Sarker, B.; Zehnder, T.; Rath, S. N.; Horch, R. E.; Kneser, U.; Detsch, R.; Boccaccini, A. R. Oxidized Alginate-Gelatin Hydrogel: A Favorable Matrix for Growth and Osteogenic Differentiation of Adipose-Derived Stem Cells in 3D. *ACS Biomater. Sci. Eng.* **2017**, *3*, 1730–1737.
- (12) Vinatier, C.; Guicheux, J. Cartilage Tissue Engineering: From Biomaterials and Stem Cells to Osteoarthritis Treatments. *Ann. Phys. Rehabil. Med.* **2016**, *59*, 139–144.
- (13) Calikoglu Koyuncu, A. C.; Gurel Pekozer, G.; Ramazanoglu, M.; Torun Kose, G.; Hasirci, V. Cartilage Tissue Engineering on

Macroporous Scaffolds Using Human Tooth Germ Stem Cells. *J. Tissue Eng. Regen. Med.* **2017**, *11*, 765–777.

(14) Sophia Fox, A. J.; Bedi, A.; Rodeo, S. A. The Basic Science of Articular Cartilage: Structure, Composition, and Function. *Sports Health* **2009**, *1*, 461–468.

(15) Gentili, C.; Cancedda, R. Cartilage and Bone Extracellular Matrix. *Curr. Pharm. Des.* **2009**, *15*, 1334–1348.

(16) Freudenberg, U.; Liang, Y.; Kiick, K. L.; Werner, C. Glycosaminoglycan-Based Biohybrid Hydrogels: A Sweet and Smart Choice for Multifunctional Biomaterials. *Adv. Mater.* **2016**, *28*, 8861–8891.

(17) Rnjak-Kovacina, J.; Tang, F.; Whitelock, J. M.; Lord, M. S. Glycosaminoglycan and Proteoglycan-Based Biomaterials: Current Trends and Future Perspectives. *Adv. Healthc. Mater.* **2018**, *7*, 1701042.

(18) Goude, M. C.; McDevitt, T. C.; Temenoff, J. S. Chondroitin Sulfate Microparticles Modulate Transforming Growth Factor- β . *Cells Tissues Organs* **2014**, *199*, 117–130.

(19) Kim, H. D.; Lee, E. A.; An, Y.-H.; Kim, S. L.; Lee, S. S.; Yu, S. J.; Jang, H. L.; Nam, K. T.; Im, S. G.; Hwang, N. S. Chondroitin Sulfate-Based Biomaterializing Surface Hydrogels for Bone Tissue Engineering. *ACS Appl. Mater. Interfaces* **2017**, *9*, 21639–21650.

(20) Sawatjui, N.; Limpaboon, T.; Schrobback, K.; Klein, T. Biomimetic Scaffolds and Dynamic Compression Enhance the Properties of Chondrocyte- and MSC-Based Tissue-Engineered Cartilage. *J. Tissue Eng. Regen. Med.* **2018**, *12*, 1220–1229.

(21) Li, T.; Song, X.; Weng, X.; Wang, X.; Sun, L.; Gong, X.; Yang, L.; Chen, C. Self-Crosslinking and Injectable Chondroitin Sulfate/Pullulan Hydrogel for Cartilage Tissue Engineering. *Appl. Mater. Today* **2018**, *10*, 173–183.

(22) Schminke, B.; Miosge, N. Cartilage Repair In Vivo: The Role of Migratory Progenitor Cells. *Curr. Rheumatol. Rep.* **2014**, *16*, 1–8.

(23) Honarpardaz, A.; Irani, S.; Pezeshki-Modaress, M.; Zandi, M.; Sadeghi, A. Enhanced Chondrogenic Differentiation of Bone Marrow Mesenchymal Stem Cells on Gelatin/Glycosaminoglycan Electrospun Nanofibers with Different Amount of Glycosaminoglycan. *J. Biomed. Mater. Res. Part A* **2019**, *107*, 38–48.

(24) Costantini, M.; Idaszek, J.; Szöke, K.; Jaroszewicz, J.; Dentini, M.; Barbeta, A.; Brinckmann, J. E.; Świąszkowski, W. 3D Bioprinting of BM-MSCs-Loaded ECM Biomimetic Hydrogels for in Vitro Neocartilage Formation. *Biofabrication* **2016**, *8*, 035002.

(25) Billiet, T.; Vandenhaute, M.; Schelfhout, J.; Van Vlierberghe, S.; Dubrue, P. A Review of Trends and Limitations in Hydrogel-Rapid Prototyping for Tissue Engineering. *Biomaterials* **2012**, *33*, 6020–6041.

(26) Song, F.; Li, X.; Wang, Q.; Liao, L.; Zhang, C. Nanocomposite Hydrogels and Their Applications in Drug Delivery and Tissue Engineering. *J. Biomed. Nanotechnol.* **2015**, *11*, 40–52.

(27) Mehrali, M.; Thakur, A.; Pennisi, C. P.; Talebian, S.; Arpanaei, A.; Nikkha, M.; Dolatshahi-Pirouz, A. Nanoreinforced Hydrogels for Tissue Engineering: Biomaterials That Are Compatible with Load-Bearing and Electroactive Tissues. *Adv. Mater.* **2017**, *29*, 1603612.

(28) Dreyer, D. R.; Todd, A. D.; Bielawski, C. W. Harnessing the Chemistry of Graphene Oxide. *Chem. Soc. Rev.* **2014**, *43*, 5288–5301.

(29) Dasari Shareena, T. P.; McShan, D.; Dasmahapatra, A. K.; Tchounwou, P. B. A Review on Graphene-Based Nanomaterials in Biomedical Applications and Risks in Environment and Health. *Nano-Micro Lett.* **2018**, *10*, 53.

(30) Pan, C.; Liu, L.; Gai, G. Recent Progress of Graphene-Containing Polymer Hydrogels: Preparations, Properties, and Applications. *Macromol. Mater. Eng.* **2017**, *302*, 1700184.

(31) Hu, Y.; Han, W.; Huang, G.; Zhou, W.; Yang, Z.; Wang, C. Highly Stretchable, Mechanically Strong, Tough, and Self-Recoverable Nanocomposite Hydrogels by Introducing Strong Ionic Coordination Interactions. *Macromol. Chem. Phys.* **2016**, *217*, 2717–2725.

(32) Rojas-Andrade, M. D.; Chata, G.; Rouholiman, D.; Liu, J.; Saltikov, C.; Chen, S. Antibacterial Mechanisms of Graphene-Based Composite Nanomaterials. *Nanoscale* **2017**, *9*, 994–1006.

(33) Mohammadrezaei, D.; Golzar, H.; Rezai Rad, M.; Omidi, M.; Rashedi, H.; Yazdian, F.; Khojasteh, A.; Tayebi, L. In vitro effect of graphene structures as an osteoinductive factor in bone tissue engineering: A systematic review. *J. Biomed. Mater. Res.—Part A* **2018**, *106*, 2284–2343.

(34) Kim, J.; Yang, K.; Lee, J. S.; Hwang, Y. H.; Park, H.-J.; Park, K. I.; Lee, D. Y.; Cho, S.-W. Enhanced Self-Renewal and Accelerated Differentiation of Human Fetal Neural Stem Cells Using Graphene Oxide Nanoparticles. *Macromol. Biosci.* **2017**, *17*, 1600540.

(35) Patel, M.; Moon, H. J.; Ko, D. Y.; Jeong, B. Composite System of Graphene Oxide and Polypeptide Thermogel As an Injectable 3D Scaffold for Adipogenic Differentiation of Tonsil-Derived Mesenchymal Stem Cells. *ACS Appl. Mater. Interfaces* **2016**, *8*, S160–S169.

(36) Shen, H.; Lin, H.; Sun, A. X.; Song, S.; Zhang, Z.; Dai, J.; Tuan, R. S. Chondroinductive Factor-Free Chondrogenic Differentiation of Human Mesenchymal Stem Cells in Graphene Oxide-Incorporated Hydrogels. *J. Mater. Chem. B* **2018**, *6*, 908–917.

(37) Zhou, X.; Nowicki, M.; Cui, H.; Zhu, W.; Fang, X.; Miao, S.; Lee, S.-J.; Keidar, M.; Zhang, L. G. 3D Bioprinted Graphene Oxide-Incorporated Matrix for Promoting Chondrogenic Differentiation of Human Bone Marrow Mesenchymal Stem Cells. *Carbon* **2017**, *116*, 615–624.

(38) Enochson, L.; Brittberg, M.; Lindahl, A. Optimization of a Chondrogenic Medium through the Use of Factorial Design of Experiments. *Biores. Open Access* **2012**, *1*, 306–313.

(39) Van Der Kraan, P. M. The changing role of TGF β in healthy, ageing and osteoarthritic joints. *Nat. Rev. Rheumatol.* **2017**, *13*, 155–163.

(40) Janssen, J. N.; Batschkus, S.; Schimmel, S.; Bode, C.; Schminke, B.; Miosge, N. The Influence of TGF- β 3, EGF, and BGN on SOX9 and RUNX2 Expression in Human Chondrogenic Progenitor Cells. *J. Histochem. Cytochem.* **2019**, *67*, 117–127.

(41) Drabsch, Y.; Ten Dijke, P. TGF- β signalling and its role in cancer progression and metastasis. *Cancer Metastasis Rev* **2012**, *31*, 553–568.

(42) Schindelin, J.; Arganda-Carreras, I.; Frise, E.; Kaynig, V.; Longair, M.; Pietzsch, T.; Preibisch, S.; Rueden, C.; Saalfeld, S.; Schmid, B.; et al. Fiji: An Open-Source Platform for Biological-Image Analysis. *Nat. Methods* **2012**, *9*, 676–682.

(43) García-Lizarribar, A.; Fernández-Garibay, X.; Velasco-Mallorquí, F.; Castaño, A. G.; Samitier, J.; Ramon-Azcon, J. Composite Biomaterials as Long-Lasting Scaffolds for 3D Bioprinting of Highly Aligned Muscle Tissue. *Macromol. Biosci.* **2018**, *18*, 1800167.

(44) Xin, G.; Yao, T.; Sun, H.; Scott, S. M.; Shao, D.; Wang, G.; Lian, J. Highly Thermally Conductive and Mechanically Strong Graphene Fibers. *Science* **2015**, *349*, 1083–1087.

(45) Li, H.; Liu, S.; Lin, L. Rheological Study on 3D Printability of Alginate Hydrogel and Effect of Graphene Oxide. *Int. J. Bioprinting* **2016**, *2*, 54–66.

(46) Zheng, J.; Zhu, M.; Ferracci, G.; Cho, N.-J.; Lee, B. H. Hydrolytic Stability of Methacrylamide and Methacrylate in Gelatin Methacryloyl and Decoupling of Gelatin Methacrylamide from Gelatin Methacryloyl through Hydrolysis. *Macromol. Chem. Phys.* **2018**, *219*, 1800266.

(47) Krishnamoorthy, K.; Veerapandian, M.; Yun, K.; Kim, S.-J. The Chemical and Structural Analysis of Graphene Oxide with Different Degrees of Oxidation. *Carbon* **2013**, *53*, 38–49.

(48) Xu, Z.; Gao, C. Aqueous Liquid Crystals of Graphene Oxide. *ACS Nano* **2011**, *5*, 2908–2915.

(49) Van Der Asdonk, P.; Kouwer, P. H. J. Liquid Crystal Templating as an Approach to Spatially and Temporally Organise Soft Matter. *Chem. Soc. Rev.* **2017**, *46*, S935–S949.

(50) Liu, Y.; Xu, Z.; Gao, W.; Cheng, Z.; Gao, C. Graphene and Other 2D Colloids: Liquid Crystals and Macroscopic Fibers. *Adv. Mater.* **2017**, *29*, 1606794.

(51) Somo, S. I.; Langert, K.; Yang, C.-Y.; Vaicik, M. K.; Ibarra, V.; Appel, A. A.; Akar, B.; Cheng, M.-H.; Brey, E. M. Synthesis and

Evaluation of Dual Crosslinked Alginate Microbeads. *Acta Biomater.* **2018**, *65*, 53–65.

(52) Olate, F. A.; Ulloa, J. A.; Vergara, J. M.; Sánchez, S. A.; Barberá, J.; Parra, M. L. Columnar Liquid Crystalline Tris-(Ether)Triazines with Pendant 1,3,4-Thiadiazole Groups: Synthesis, Mesomorphic, Luminescence, Solvatofluorochromic and Electrochemical Properties. *Liq. Cryst.* **2016**, *43*, 811–827.

(53) Buyuktanir, E. A.; Frey, M. W.; West, J. L. Self-Assembled, Optically Responsive Nematic Liquid Crystal/Polymer Core-Shell Fibers: Formation and Characterization. *Polymer* **2010**, *51*, 4823–4830.

(54) Abedin, M. J.; Gamot, T. D.; Martin, S. T.; Ali, M.; Hassan, K. I.; Mirshekarloo, M. S.; Tabor, R. F.; Green, M. J.; Majumder, M. Graphene Oxide Liquid Crystal Domains: Quantification and Role in Tailoring Viscoelastic Behavior. *ACS Nano* **2019**, *13*, 8957–8969.

(55) Hong, S.-H.; Shen, T.-Z.; Song, J.-K. Flow-Induced Ordering of Particles and Flow Velocity Profile Transition in a Tube Flow of Graphene Oxide Dispersions. *Liq. Cryst.* **2015**, *42*, 261–269.

(56) Tan, Y.; Wang, L.; Xiao, J.; Zhang, X.; Wang, Y.; Liu, C.; Zhang, H.; Liu, C.; Xia, Y.; Sui, K. Synchronous Enhancement and Stabilization of Graphene Oxide Liquid Crystals: Inductive Effect of Sodium Alginates in Different Concentration Zones. *Polymer* **2019**, *160*, 107–114.

(57) Chen, S.; Li, R.; Li, X.; Xie, J. Electrospinning: An Enabling Nanotechnology Platform for Drug Delivery and Regenerative Medicine. *Adv. Drug Deliv. Rev.* **2018**, *132*, 188–213.

(58) Gao, Y.; Mori, T.; Manning, S.; Zhao, Y.; Nielsen, A. D.; Neshat, A.; Sharma, A.; Mahnen, C. J.; Everson, H. R.; Crotty, S.; et al. Biocompatible 3D Liquid Crystal Elastomer Cell Scaffolds and Foams with Primary and Secondary Porous Architecture. *ACS Macro Lett.* **2016**, *5*, 4–9.

(59) Mackay, M. E.; Dao, T. T.; Tuteja, A.; Ho, D. L.; Van Horn, B.; Kim, H.-C.; Hawker, C. J. Nanoscale Effects Leading to Non-Einstein-like Decrease in Viscosity. *Nat. Mater.* **2003**, *2*, 762–766.

(60) Jain, S.; Goossens, J. G. P.; Peters, G. W. M.; van Duin, M.; Lemstra, P. J. Strong Decrease in Viscosity of Nanoparticle-Filled Polymer Melts through Selective Adsorption. *Soft Matter* **2008**, *4*, 1848.

(61) Rathan, S.; Dejob, L.; Schipani, R.; Haffner, B.; Möbius, M. E.; Kelly, D. J. Fiber Reinforced Cartilage ECM Functionalized Bioinks for Functional Cartilage Tissue Engineering. *Adv. Healthc. Mater.* **2019**, *8*, 1801501.

(62) Chen, Y.; Wang, Y.; Yang, Q.; Liao, Y.; Zhu, B.; Zhao, G.; Shen, R.; Lu, X.; Qu, S. A Novel Thixotropic Magnesium Phosphate-Based Bioink with Excellent Printability for Application in 3D Printing. *J. Mater. Chem. B* **2018**, *6*, 4502–4513.

(63) Sarker, B.; Singh, R.; Silva, R.; Roether, J. A.; Kaschta, J.; Detsch, R.; Schubert, D. W.; Cicha, I.; Boccaccini, A. R. Evaluation of Fibroblasts Adhesion and Proliferation on Alginate-Gelatin Cross-linked Hydrogel. *PLoS One* **2014**, *9*, No. e107952.

(64) Kenry; Lim, C. T. Biocompatibility and Nanotoxicity of Layered Two-Dimensional Nanomaterials. *ChemNanoMat* **2017**, *3*, 5–16.

(65) Goenka, S.; Sant, V.; Sant, S. Graphene-Based Nanomaterials for Drug Delivery and Tissue Engineering. *J. Control. Release* **2014**, *173*, 75–88.

(66) Nair, M.; Nancy, D.; Krishnan, A. G.; Anjusree, G. S.; Vadukumpully, S.; Nair, S. V. Graphene oxide nanoflakes incorporated gelatin-hydroxyapatite scaffolds enhance osteogenic differentiation of human mesenchymal stem cells. *Nanotechnology* **2015**, *26*, 161001.

(67) Saravanan, S.; Vimalraj, S.; Anuradha, D. Chitosan Based Thermoresponsive Hydrogel Containing Graphene Oxide for Bone Tissue Repair. *Biomed. Pharmacother.* **2018**, *107*, 908–917.

(68) Garcia-Alegria, E.; Iliut, M.; Stefanska, M.; Silva, C.; Heeg, S.; Kimber, S. J.; Kouskoff, V.; Lacaud, G.; Vijayaraghavan, A.; Batta, K. Graphene Oxide Promotes Embryonic Stem Cell Differentiation to Haematopoietic Lineage. *Sci. Rep.* **2016**, *6*, 25917.

(69) Varghese, S.; Hwang, N. S.; Canver, A. C.; Theprungsirikul, P.; Lin, D. W.; Elisseeff, J. Chondroitin Sulfate Based Niches for Chondrogenic Differentiation of Mesenchymal Stem Cells. *Matrix Biol.* **2008**, *27*, 12–21.

(70) Andrews, S. H. J.; Kunze, M.; Mulet-Sierra, A.; Williams, L.; Ansari, K.; Osswald, M.; Adesida, A. B. Strategies to Mitigate Variability in Engineering Human Nasal Cartilage. *Sci. Rep.* **2017**, *7*, 6490.